https://doi.org/10.5194/egusphere-2025-455
Preprint. Discussion started: 18 February 2025

A Novel Identification Method for Stratospheric Gravity Waves in Nadir Viewing Satellite Observations

Peter G. Berthelemy[1], Corwin J. Wright[1], Neil P. Hindley[1], Phoebe E. Noble[1], and Lars Hoffmann[2]

[1]Centre for Climate Adaptation and Environment Research, University of Bath, Bath, UK
[2]Jülich Supercomputing Center, Forschungszentrum Jülich, Jülich, Germany, Jülich, Germany

Correspondence: Peter G. Berthelemy (pb948@bath.ac.uk)

Abstract. Atmospheric gravity waves (GWs) are an important mechanism for vertical transport of energy and momentum through the atmosphere. Their impacts are apparent at all scales including aviation, weather, and climate. Identifying stratospheric GWs from satellite observations is challenging due to instrument noise and effects of weather processes, but they can be observed from nadir sounders such as the AIRS instrument onboard Aqua. Here, a new method (hereafter 'neighbourhood method") to detect GW information is presented and applied to AIRS data. We describe the concept of the neighbourhood method and use it to investigate GW amplitudes, zonal pseudomomentum fluxes, and vertical wavelengths over 5 years of AIRS data. We compare these results to those calculated from GWs detected using another widely used method based on a defined amplitude cutoff. The neighbourhood method reveals GW patterns in seasonal means that are not visible when using the amplitude cutoff method. Time series analysis suggests that GWs have a larger impact than was previously analysed from the amplitude cutoff detection method. $\sim 25\%$ of waves detected using the neighbourhood method have amplitudes lower than is visible using the amplitude cutoff method. Three regions are studied in greater depth: the Rocky Mountains, North Africa, and New Zealand/Tasmania. GWs detected using the neighbourhood method have realistic wave phase propagation angles, which are consistent with surface-levels winds from ERA5 climatological reanalyses. Using the neighbourhood method produces new statistics for regional and global GW studies, which compares favourably to the amplitude cutoff GW detection method.

1 Introduction

Atmospheric gravity waves (hereafter referred to as 'GWs') are a vital component in the dynamics of the atmosphere. They are one of the main processes by which energy and momentum are transferred vertically through the atmosphere (Holton, 1982), and as such can have large impacts on aviation, atmospheric chemistry, the general circulation, and other atmospheric phenomena. GWs propagate throughout the atmosphere, but have their largest effects at higher altitudes, as they increase in amplitude with height because of the exponential drop in pressure. They are generated by a wide array of mechanisms, with by far the two most important being flow over orography and deep convection (Smith and Lyjak, 1985; Tsuda et al., 1994; Fritts and Alexander, 2003; Achatz et al., 2024). Other mechanisms include geostrophic adjustments from jet streams (Fritts and Alexander, 2003) and frontal systems (Plougonven and Teitelbaum, 2003; Zhang, 2004), and non-linear wave-wave interactions.

These diverse mechanisms can lead to large differences in the waves they produce, but the vast majority of GWs have horizontal wavelengths up to thousands of kilometres (Choi et al., 2012; Kalisch et al., 2016; Trinh, 2016; Hájková and Šácha, 2023), and horizontal packet sizes ranging from less than 10 km up to many hundreds of kilometres (Fritts et al., 2016). GWs generated through these mechanisms have periods ranging from hours to days (Dunkerton, 1982; Baldwin et al., 2001; Ern et al., 2021).

The wide range of periods and wavelengths that GWs have make it difficult for instruments to observe the whole spectrum, an issue often referred to as the 'observational filter' problem (Preusse et al., 2002; Alexander et al., 2010). For example, nadir-sounding satellite instruments are usually good at resolving fine-scale horizontal wavelength waves due to their high horizontal sampling and fine measurement resolution, but as a trade-off usually have coarse vertical resolution.

The Atmospheric Infrared Sounder (AIRS) instrument onboard Aqua, a Sun-synchronous polar orbiting satellite, is a nadir-sounding instrument that scans across-track. This allows for 3D measurements of GWs. AIRS has been used for many GW studies over its near-22 year life to date (Alexander and Teitelbaum, 2007; Hoffmann et al., 2013; Gong et al., 2015; Hoffmann et al., 2016; Wright et al., 2016, 2017). Previous studies using AIRS data have used various approaches to study the GWs present. Hoffmann et al. (2013) used a technique to detect GWs where the variance of each AIRS temperature perturbation footprint was calculated from all footprints within a 100 km radius. If this variance was larger than a defined cutoff then the footprint was deemed to contain a GW. Hoffmann et al. (2016) improved on this by taking variance differences between two boxes, one over an orographic hotspot and the other upwind of the hotspot. This was used to identify whether orographically-generated GWs exhibited larger variances downstream of the mountain than upstream. Finally, Ern et al. (2017) used an amplitude-cutoff approach to extract GWs from AIRS data, allowing them to study waves using the S3D technique (Lehmann et al., 2012).

Previous work has also used the S-transform (Stockwell et al., 1996), hereafter referred to as the ST (Hindley et al., 2016; Wright et al., 2017; Hindley et al., 2019), to detect GWs. This resembles a continuous wavelet transform combined with with a complex sinusoidal wavelet windowed with a scalable Gaussian (Gibson et al., 2006). This provides localised frequency space information about an input signal. Such an analysis assumes that a wave is present at all locations in the data, and so will fit wave properties even if there is no wave. When no wave is actually present, such ST analyses generally assign low amplitudes to the associated voxels, which is why the amplitude cutoff method is able to detect strong high-amplitude waves. However, since the ST uses information from many points, it can in principle accurately characterise GWs that have amplitudes lower than the AIRS pointwise thermal noise. The amplitude cutoff method would not be able to detect these low amplitude GWs without setting a cutoff level low enough to pass noise features through the analysis, and as such a method that is not based on the amplitude properties of the waves is useful to permit the identification of low-amplitude GWs.

In this study, we describe such a new method to detect stratospheric GWs in AIRS observations. This method uses an S-transform to calculate wave properties, and then identifies GWs using these properties. Section 2 and Section 3 describes AIRS and the steps we use to identify waves in the ST output, respectively, including a brief description of how we preprocess the AIRS data. This involves applying the ST to the data, identifying areas of stable spatial horizontal wavenumbers, and creating a binary mask over these areas identifying whether a wave has been detected or not. In Section 4, we explore differences

https://doi.org/10.5194/egusphere-2025-455
Preprint. Discussion started: 18 February 2025

between results obtained using this method and an amplitude cutoff approach, focusing on both global and local differences. To demonstrate these differences three regions are analysed, specifically (i) the Rocky Mountains, (ii) North Africa, and (iii) New Zealand and Tasmania. Finally, we draw conclusions in Section 5.

2 Data

AIRS (the Atmospheric InfraRed Sounder) (Aumann et al., 2003; Chahine et al., 2006) is one of six remote sensing instruments aboard NASA's Aqua satellite. Aqua was launched in May 2002 into a Sun-synchronous polar orbit. AIRS provides derived global measurements of temperature, humidity, and greenhouse gases. The data collected by AIRS has contributed significantly to climate research, weather forecasting, and atmospheric science more generally (Marshall et al., 2006). AIRS measures atmospheric radiances over a spectral range of 3.74 – 15.4 μm using 2378 infrared channels, which can be used to characterise the Earth's atmosphere at different altitudes. The instrument scans in the nadir, with each cross-track scan covering $\sim$1765 km on the ground, split between 90 footprints, with a complete scan taking 2.67 seconds. Due to the nadir-sensing geometry and constant angular velocity of the scan, across-track resolution is higher at swath centre and coarser at swath edge (Hoffmann et al., 2014). The cross-track sampling distance varies between 13 km at nadir and 42 km at the scan edges. The distance along-track between consecutive scans is 18 km, and each set of 135 scans is stored independently as a 'granule'. The instrument provides near-global coverage during its 14.5 daily orbits.

In this study, we use 3D AIRS stratospheric temperature data, retrieved using the method of Hoffmann and Alexander (2009). This retrieval uses radiance measurements at 4.3 and 15 μm, where the observed radiance originates in the stratosphere (Alexander and Barnet, 2007; Hoffmann and Alexander, 2009). The radiative transfer model used for the retrieval retains the horizontal resolution from the original radiance data in the across- and along-track directions (Alexander and Teitelbaum, 2007). The vertical resolution of the retrievals is 7 – 15 km, varying depending on altitude. The majority of uncertainty in the stratosphere is retrieval noise, which varies between 1.4 – 2.1 K. Both the vertical resolution and the uncertainty are illustrated by Figure 2 of Hindley et al. (2019).

This retrieval assumes local thermodynamic equilibrium (LTE), meaning two schemes are needed, one for nighttime and one for daytime. The nighttime scheme uses both 4.3 and 15 μm measurements, which are both valid under the assumption of LTE. During daytime, non-LTE effects arise in the 4.3 μm measurements from solar excitation, so only the 15 μm measurements are used in this scheme. Note that the daytime scheme does have larger retrieval noise than the nighttime scheme, for more information see Figure 2 in Hindley et al. (2019).

3 Methods

3.1 Preprocessing

Each granule of the retrieved temperatures for each day is linearly interpolated onto a regular distance grid of 128×135 pixels at each height level to support our spectral analysis. An across-track spacing of 128 pixels is used as it is efficient for Fourier analysis, a key part of the spectral analysis applied later. When regridded, the resolution across-track is ∼14 km, which is representative of the original resolution at track-centre but is approximately a threefold oversampling at track-edge. We do not smooth the data before analysis.

Planetary-scale waves and large temperature fluctuations are removed using a fourth-order polynomial in the across-track direction at each height level, which is a widely used technique for separating GWs from planetary-scale waves and large scale background temperatures when working with AIRS data (Wu, 2004; Hindley et al., 2019; Wright et al., 2021). The remaining temperature perturbations are assumed to be GWs. Nyquist's theorem, along with a sampling footprint distance of 14 km, limits the horizontal wavelengths we can measure in these observations to ∼30 km at nadir, and ∼80 km at track-edge. The data after the fourth-order polynomial detrending is sensitive to GWs with relatively short horizontal wavelengths (< 600 km) and long vertical wavelengths (∼15 km). Hoffmann et al. (2014), Ern et al. (2017) and Hindley et al. (2019) provide more information on the scales of GWs resolved by this dataset.

3.2 S - Transform Method

The ST is then applied to two granules at a time (270 cross-track rows, around 12 minutes of data) of the temperature perturbations, and the properties of the dominant wave in each voxel are characterised. We use a modified ST to achieve this, which combines the approaches of the 3DST described by Hindley et al. (2019) and applied by Wright et al. (2017), and the 2D+1ST approach later described by Wright et al. (2021). We first apply a 3DST to the full three-dimensional dataset, then apply the 2D+1ST approach as described by Wright et al. (2021) with an additional restriction to detect only those spatial frequencies with the greatest spectral magnitude in the 3DST output. This allows us to benefit from the improved vertical wavelength discrimination of the 2D+1ST, while also retaining the robustness to noise of the 3DST.

We limit our analysis to along-track and cross-track wavelengths of values greater than 25 km, while vertical wavelengths are restricted to values greater than 6 km. These limits are chosen in order to constrain the detected waves to those well-resolved by the Hoffmann and Alexander (2009) AIRS retrieval (Hindley et al., 2019). We make the assumption that all GWs propagate upwards, rather than downwards so that ambiguity of propagation direction is broken. To do so, we specifically set all vertical wavenumbers to be negative (Hindley et al., 2019).

Following this, the 39 km altitude level is selected for postprocessing to identify waves present in the data. This altitude level was selected because it lies within the region of highest resolution and lowest total noise in the 3D temperature retrieval of Hoffmann and Alexander (2009) (Ern et al., 2017; Hindley et al., 2019). The following wave detection method can be applied in the same way to other levels within AIRS that have the same resolution and total noise. It could be applied to other levels, but the variables within the neighbourhood method would have to be adjusted to best suit the final results.

3.3 Wave Detection

We next apply the neighbourhood method to detect regions that contain GWs, so that we can use these GW properties in further analysis, and measurements from regions with no GWs. The fundamental principle of this method is that we expect GWs to have similar wave properties between adjacent pixels, or over pixels in a local 'neighbourhood' (Wright et al., 2017;

Hindley et al., 2019; Lear et al., 2023). Regions containing random noise are instead expected to have randomly changing wave properties over the same neighbourhoods.

Areas of consistent wave properties at 39 km altitude are identified using the following methodology:

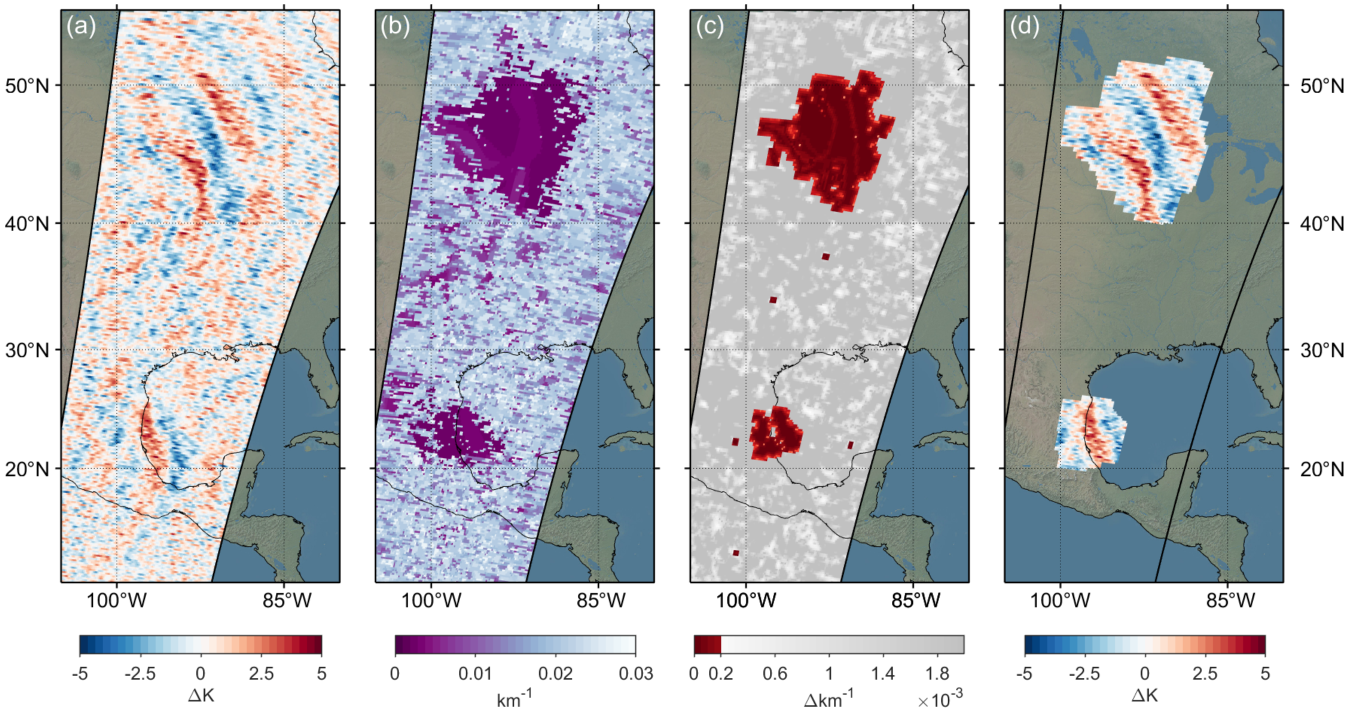

Figure 1. Step-by-step masking of two waves over North America, July 17th, 2010, granules 80 – 83. From left to right: (a) The temperature perturbations after preprocessing. (b) The horizontal wavenumbers found from the ST; the regions where the waves can be visually seen in the temperature perturbations appear as regions of similar wavenumber. (c) The average absolute difference between horizontal wavenumbers within each pixel's neighbourhood, the red indicates everywhere lower than the cutoff (2×10^{-4} km^{-1}). (d) The final mask applied to the original temperature perturbations.

(a) Pairs of granules are concatenated in the along-track direction (Figure 1a.).

(b) The ST is applied, and the output used to identify the dominant wave amplitude and along-track, cross-track and vertical wavenumbers for each voxel, which are then projected into zonal, meridional, and vertical wavenumbers *k, l, m*. From this, it can be seen that GWs appear as regions of similar horizontal wavenumber amongst the noise, as illustrated by Figure 1b.

(c) For each pixel, the mean absolute difference between the horizontal wavenumbers of each pixel and the pixels in its 5×5 pixel adjacency neighbourhood is calculated. (Figure 1c.). The reasoning for the size of the neighbourhood is discussed in Appendix A1.

https://doi.org/10.5194/egusphere-2025-455
Preprint. Discussion started: 18 February 2025

(d) We apply a maximum tolerance of $C = 2 \times 10^{-4}$ km^{-1} to this mean absolute difference field. Regions where assigned values are lower than this cutoff indicate that horizontal wavenumbers in the region are not varying significantly spatially, which is consistent with our expectation of a GW.

(e) Finally, contiguous positive-detection regions with an area smaller than three times the area of the neighbourhood (i.e. 75 voxels) are then removed from our dataset. This is to ensure that only plausible waves are detected, and removes small areas of coherent wavenumber noise (see Appendix A2 for more information).

This methodology creates a binary mask, which can be applied to any wave parameter, such as in Figure 1d.

We have carried out a range of sensitivity tests for the values of the spatial wavenumber difference cutoff and the size of the neighbourhood analysed, which are discussed in Appendix A1. We also discuss the selection of the cutoff value used in Appendix A2; based on these tests, we conclude that while the optimum value of the tolerance cutoff does inherently depend on the individual wave present in the data, 2×10^{-4} km^{-1} represents a good compromise well-suited to the majority of waves present in our test cases.

The zonal pseudomomentum flux (momentum flux, or MF) is then calculated for each point where a wave is detected using Equation 1. MF is a derived value that characterises how much momentum is being transported by a GW (Fritts and Alexander, 2003; Ern et al., 2004), and thus how much potential drag (Ern et al., 2016) the waves have. Accurate estimates of MF are needed so that models can more precisely parameterise GWs. As derived by Ern et al. (2004), this can be calculated as:

$$(\mathrm{MF}_x, \mathrm{MF}_y) = \frac{\rho}{2}\left(\frac{g}{N}\right)^2\left(\frac{A}{BG}\right)^2\left(\frac{k}{m}, \frac{l}{m}\right) \tag{1}$$

where ρ, g and N are density, acceleration due to gravity (9.81 ms^{-2}), and the Brunt–Väisälä frequency (0.02 s^{-1}), respectively, A and BG are the amplitude of the GW and the background temperature. k, l and m are the horizontal and vertical wavenumbers that describe the wave.

4 Results

We compare the results from using the neighbourhood method to the results from using the amplitude cutoff method, here using a cutoff of 1.6 K that is categorised as the retrieval error from Hoffmann and Alexander (2009) and selected in previous GW studies Hindley et al. (2020). Any points which have a value less than this are classified as noise, and are removed from our analysis.

Figure 2 shows a global comparison between the amplitude cutoff method and the neighbourhood method. Specifically, it shows the mean amplitudes of detected GWs during local winter months, November-February (NDJF) for the Northern hemisphere and June-September (JJAS) for the Southern hemisphere. The differences (g, h, i) and ratios (j, k, l) between the two methods are also presented.

In most areas where GWs are detected using both methods, the mean amplitude from GWs detected using the neighbourhood method are greater than GWs detected using the amplitude cutoff method (Figure 2g-l). This is because the neighbourhood

https://doi.org/10.5194/egusphere-2025-455
Preprint. Discussion started: 18 February 2025

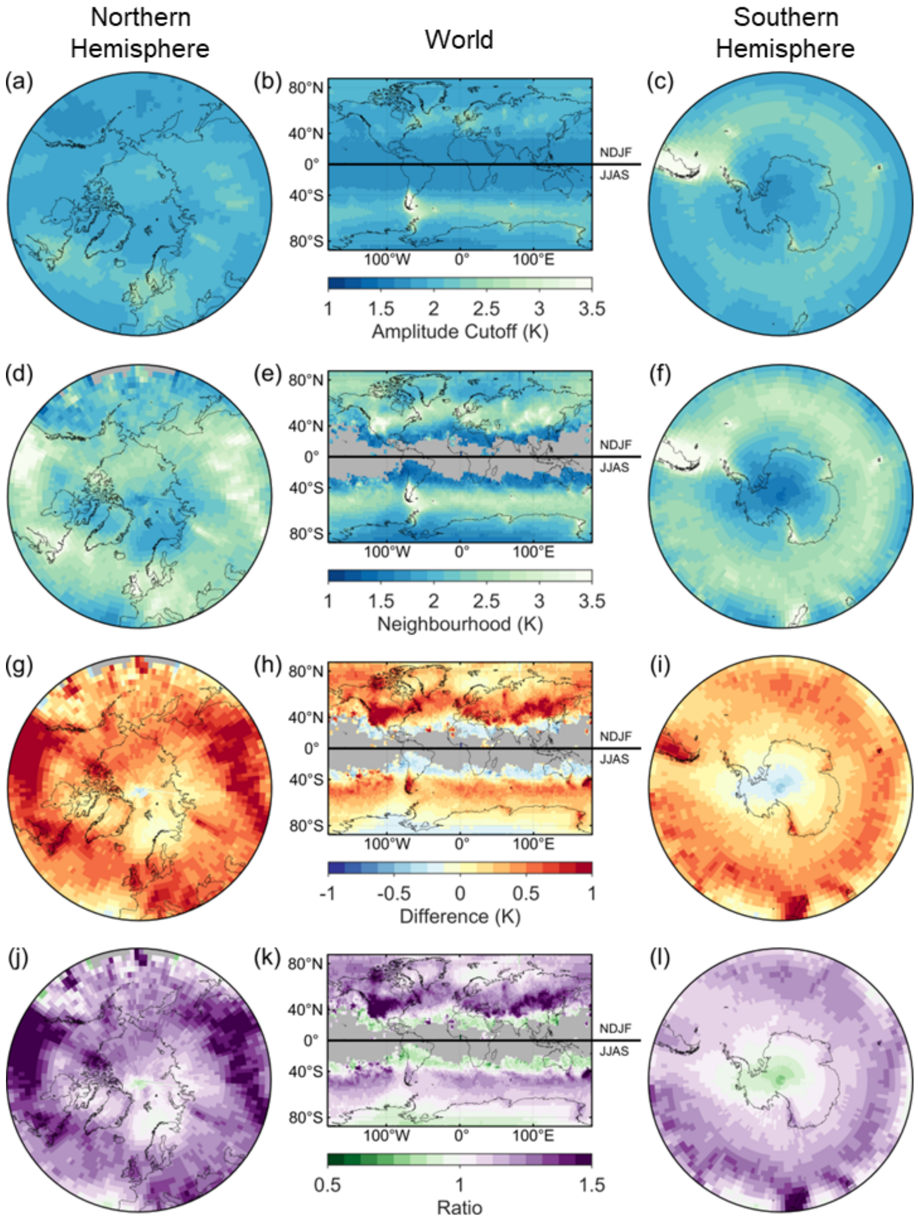

Figure 2. Maps showing mean detected GW amplitudes between 2010–2014 for local winter month in both hemispheres. (a, b, c) GWs detected using the amplitude cutoff method, (d, e, f) GWs detected using the neighbourhood method, (g, h, i) the difference between amplitudes measured using the two methods, and (j, k, l) the amplitude ratio of the two methods.

method only detects GWs, whereas the amplitude cutoff method incorporates all of the pixels with amplitudes above the defined cutoff, which can include noise. This brings the mean of the amplitudes towards the mean of the noise. Over some regions that are well-known to be associated with high GW activity, such as New Zealand and Western North America (Hoffmann et al., 2013, 2016), the mean amplitude of GWs detected using the amplitude cutoff method is lower than the mean amplitude of GWs detected using the neighbourhood method.

The amplitudes of GWs associated with the lower stratospheric polar jets (Wright et al., 2017; Sato et al., 2012) are seen clearly using the neighbourhood method, especially the Northern polar jet, where a band of high amplitudes stretching from North America across to Iceland and through to Northern China can be observed (Figure 2d-f).

We see only small changes in amplitude between the two methods (Figure 2g-i) in areas associated with strong and consistent GW activity, such as over the Antarctic peninsula. This is due to the two methods both detecting the same waves, and hence converging on very similar time-mean amplitudes.

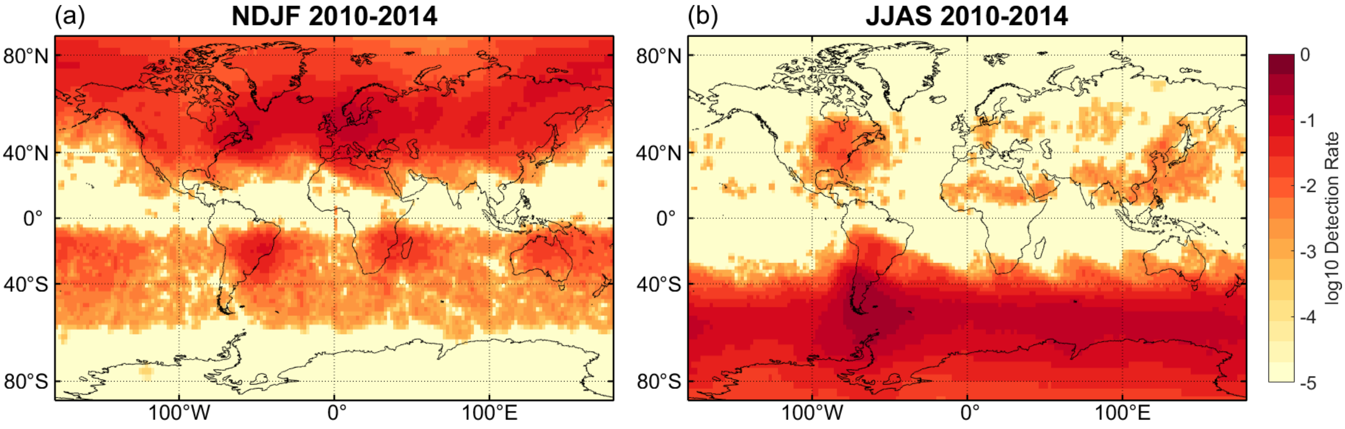

Figure 3. A map of the average wave detection rate per AIRS overpass using the neighbourhood method. (a) shows boreal winter, November-February, and (b) shows austral winter, June-September. On a log10 scale.

Figure 3 shows the occurrence rate of GWs detected using the neighbourhood method, which we define as the average number of GWs detected over a $2° \times 2°$ area per AIRS overpass. Compared to Figures 6 and 7 of Hoffmann et al. (2013) (hereafter referred to as H13), who used a temperature variance method to detect GWs, Figure 3 shows many of the same features and similar occurrence rates worldwide. There are some differences: GWs detected over the Southern Ocean in JJAS have a much higher occurrence rate in this figure than in H13, and there are waves detected nearly everywhere in the Northern hemisphere in NDJF, whereas in H13 they were more sparse. The hotspots shown in H13's Figures 14 and 15 exhibit a higher occurrence rate than that seen in our Figure 3, but they each hotspot is spatially smaller and these hotspots were spread across the world more than is seen in Figure 3. These differences might be due to the H13 detection technique characterising peak events as having GW variance exceeding the zonal mean variance.

4.1 Histograms of Latitude Bands

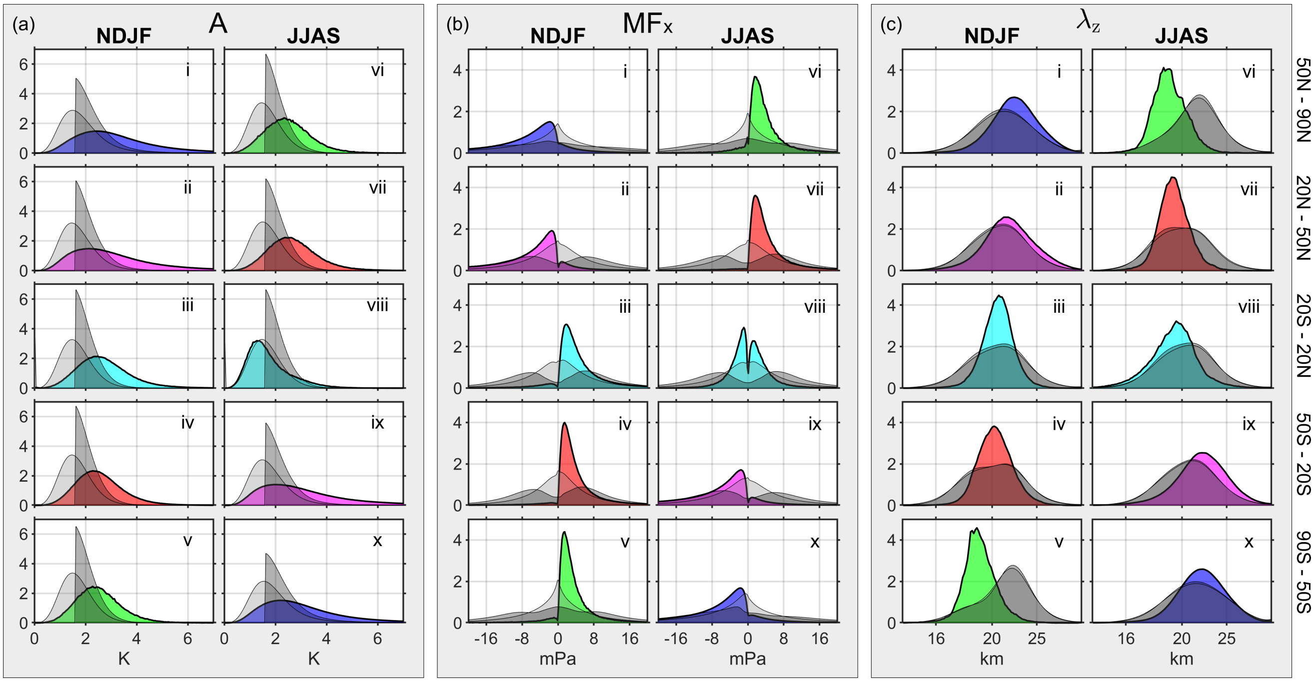

Figure 4. Histograms of latitude bands during boreal winter (NDJF, i-v) and austral winter (JJAS, vi-x) between 2010–2014, presenting amplitude (a), zonal momentum flux (b), and vertical wavelength (c). Each panel includes three histograms: light grey for waves detected using only the ST, dark grey for waves detected using the amplitude cutoff method, and coloured for waves extracted using the neighbourhood approach. Colours represent the season local to that latitude band. Each histogram has been internally normalised to sum to 100% for ease of comparison. It is noted that vertical wavelength (c) is linear in wavenumber.

Figure 4 shows histograms of GW amplitudes, zonal momentum flux, and vertical wavelengths for the three methods (i.e. ST, amplitude-cutoff and neighbourhood) of detecting GWs, in each panel for their respective season and latitude bands.

Each variable presented in Figure 4 appears to exhibit meridional changes (e.g. b. i-v) in the GWs detected using the neighbourhood method. This is equivalent to seasonal changes throughout the year. We hypothesise that this is due to both the changing winds beneath the altitude of observation (39 km), and the sources of GWs changing meridionally. These changes are seen as a movement of the curve's peak, or as a change in the width of the curve. We discuss the three variables: amplitude, zonal momentum flux, and vertical wavelength individually.

4.1.1 Amplitude (A)

Figure 4a shows the amplitudes from GWs detected using the amplitude cutoff method and the neighbourhood method, and also the amplitudes calculated from the ST with no additional detection method applied. The peaks of the histograms for waves detected using the neighbourhood method are consistently at larger amplitudes than the other two histograms, with the exception of the tropics during austral winter (Figure 4a. viii). This shows that the noise that the amplitude cutoff method includes affects the data substantially. In the tropics during austral winter, the majority (∼55%) of waves found using the neighbourhood method have amplitudes lower than the limit of the amplitude cutoff method, and hence could not be detected using it.

Strong meridional differences are apparent when using the neighbourhood method to extract amplitudes; during austral winter, the polar regions (Figure 4a. vi & x) have similar peak amplitudes (∼2.20 K), whereas in the tropics the peak lies at 1.25 K. There are a greater percentage of high amplitude GWs during local wintertime than during local summertime, with $\sim 7\times$ more waves with amplitudes larger than 6 K in local wintertime. When using only the ST to detect GWs, there is little change between latitudes and seasons, with a peak at 1.6 K in all panels, which seems to mainly characterise the noise.

4.1.2 Zonal Momentum Flux ($\mathrm{MF_x}$)

When GWs propagate into a region of wind travelling with the same speed and direction as the GW's horizontal phase speed, the wave will undergo critical level filtering (Whiteway and Duck, 1996; Booker and Bretherton, 1967). This causes the wave to break and deposit its energy and momentum into the background wind, changing the speed and direction of the background flow. The morphology of the coloured histograms presented in Figure 4b is due to this phenomenon. For example in Figure 4b. i, the waves detected using the neighbourhood method have mainly negative $\mathrm{MF_x}$, indicating that they propagate westwards. This concurs with ERA5 wind reanalysis data in this region, with the vast majority of wind being eastwards. These results agree with the findings of Hindley et al. (2020), although the values for zonal momentum flux ($\mathrm{MF_x}$) calculated using the neighbourhood method are $\sim 10\times$ greater than found in the Hindley study. The $\mathrm{MF_x}$ calculated from GWs detected using the amplitude cutoff method does not observe the same directionality of $\mathrm{MF_x}$ as when using the neighbourhood method, instead it exhibits a double-peaked curve throughout the year.

Some waves detected using the neighbourhood method have $\mathrm{MF_x}$ in the direction of the background wind. These can be attributed to a variety of causes: the waves may have propagated meridionally and evaded a critical level, there may not have been a critical level for that particular wave where the waves propagated vertically, or the 3DST may have miscalculated the angle of propagation. The 3DST issue arises when the phase fronts of the GW are aligned near to the vertical; the technique must assign the wave to be angled in some direction relative to the vertical, and if the vertical angle assigned is directly vertical to within uncertainty bounds then errors can occur.

In the tropics (Figure 4b. iii, viii), the effects of the semiannual oscillation on the GWs (Smith et al., 2017) can be seen clearly when using the neighbourhood method. The same pattern of eastwards GW activity during boreal winter and near symmetrical eastwards/westwards GW activity during austral winter is observed in the Hindley et al. (2020) study, although much greater values of $\mathrm{MF_x}$ were calculated in our study. The background winds for this can also be seen in Delisi and Dunkerton (1988). The effects of the quasi-biennial oscillation cannot be observed here, possibly due to the waves that drive it being shorter than 10 km vertically, i.e.outside the observational filter of AIRS (Hindley et al., 2020).

https://doi.org/10.5194/egusphere-2025-455
Preprint. Discussion started: 18 February 2025

The lack of signal that can be seen around 0 mPa is due to the noise floor of AIRS, as the 3DST cannot resolve very low amplitude waves, therefore the neighbourhood method can not detect the waves. Momentum flux is proportional to amplitude squared (Equation. 1), so lower amplitude waves not being included would impact upon measured MF_x values.

4.1.3 Vertical Wavelength (λ_z)

Figure 4c shows very few differences between the vertical wavelength values calculated from the amplitude cutoff method and from the data with no detection method applied. Using the neighbourhood method a seasonal cycle can be seen, the peaks shift towards shorter vertical wavelengths and the curves narrow as the local seasons change from winter to summer. For example, during boreal winter (Figure 4c. i - v) the peak location changes from 22.2 km in the north to 18.5 km in the south, a difference of 3.7 km. The full-width half maximum during this period narrows, reducing by 62% from 90°N to 90°S. The longer wavelengths seen in the winter could be due to the stronger zonal background winds that occur during wintertime. These winds allow the long vertical wavelength waves to propagate into the stratosphere (Hoffmann et al., 2013).

4.2 Regional Studies

Three regions were chosen for deeper study (Figure 5), specifically:

- the Rocky Mountains, which are a well-studied source of high GW activity (Lilly and Kennedy, 1973; Wang and Geller, 2003; Gong and Geller, 2010; Zhang et al., 2015; Wright and Banyard, 2020) with complex orography when compared to other regions (e.g. southern Andes) (Zhang et al., 2013),
- North Africa, where studies have identified the main drivers of GW in this region as the West African monsoon (Birch et al., 2012) and the Hoggar mountains (Orza et al., 2020), but in general fewer studies have been carried out specific to the region when compared to the other two regions, and
- New Zealand and Tasmania, which was previously studied during the DEEPWAVE campaign (Bossert et al., 2017; Gisinger et al., 2017). Hoffmann et al. (2016) detected GWs over this region 13.5% of the time in AIRS, with Eckermann and Wu (2012) and Pautet et al. (2019) finding that Tasmania is an important driver of GWs.

Figure 6 shows the annual cycle of GW activity over each region, where each column shows a distinct region. The top two rows (panels a – f) show the amplitudes of detected GWs for each region, with the first row (panels a – c) showing values calculated for GWs detected using the amplitude cutoff method, and the second row (panels d – f) showing values calculated from GWs detected using the neighbourhood method. The bottom two rows (panels g – l) show zonal momentum flux from GWs detected using the amplitude cutoff method (panels g – i) and the neighbourhood method (panels j – l). Each panel has been normalised to sum to 1.

Considering first the amplitudes of GWs detected using the amplitude cutoff method (panels a – c), the Rocky Mountains and New Zealand/Tasmania (panels a & c) exhibit similar morphologies, but offset by 6 months, with more higher amplitude GWs being detected during local winter, and becoming less frequent going into local summertime. This is due to the lower

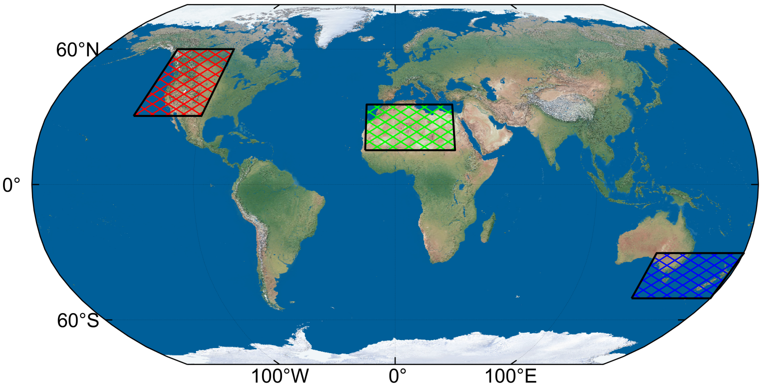

Figure 5. The regions chosen as case studies for this study. The Rocky Mountains, North Africa, and New Zealand/Tasmania

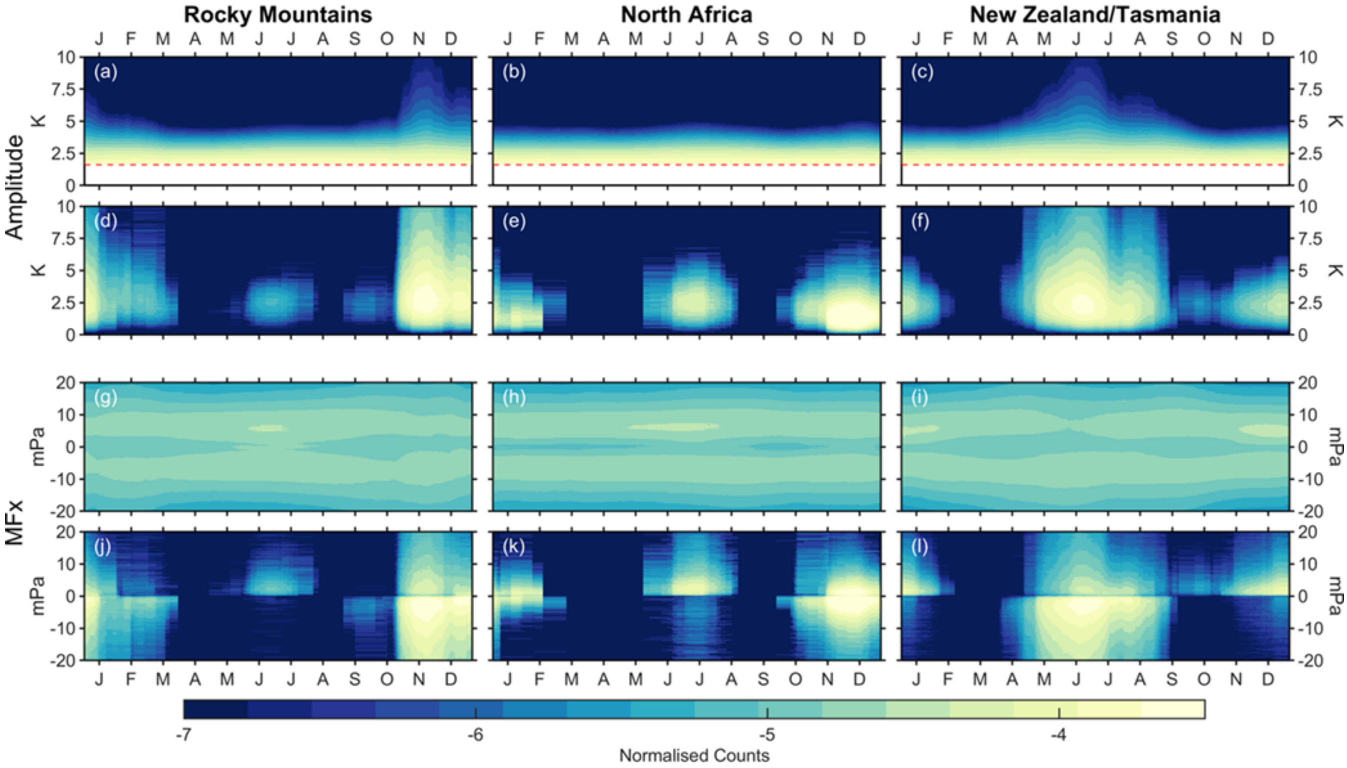

Figure 6. Histograms for each day of the year (2010–2014) over the three regions: the Rocky Mountains (a, d, g, j), North Africa (b, e, h, k), and New Zealand/Tasmania (c, f, i, l) of amplitude (a – f) and zonal momentum flux (g – l). Panels a – c and g – i present the values of waves detected using the amplitude cutoff method, and panels d – f and j – l present the values of waves detected using the neighbourhood method. Colours are on a log10 scale, and have been normalised to sum to one. The red lines on panels a – c indicates the amplitude cutoff used.

stratospheric polar jet becoming stronger and more stable during the local wintertime, allowing GWs generated lower in altitude to propagate upwards. This also indicates that these regions have similar drivers of GWs, in this case orography. Panel b, which shows the same data but for GWs over North Africa, has no distinctive enhancement of large amplitude GWs, but has similar continual low amplitude activity to the other regions.

The amplitudes of GWs detected using the neighbourhood method (panels d – f) appear to follow the same pattern as in panels a – c, but the continual low amplitude signal is not present. This allows the seasonal low amplitude GWs to become more evident, and increases the proportion of high amplitude GWs. On average, $\sim 25\%$ of the GWs detected using the neighbourhood method in these three regions have amplitudes below the amplitude cutoff and as such would not be detected using the amplitude cutoff method. There is a large difference in the fraction of waves detected using the neighbourhood method during the local summer months between the Rocky Mountains and New Zealand, with $\sim 9\times$ more GWs detected over New Zealand (panel f). This may be due to the more stable winds around the South Pole than in the North during the summer, or because of the Southern Ocean storm belt interacting with the orography in New Zealand (Chapman et al., 2015). In panel e, GW activity from the West African monsoon is observed between May and August. Wright et al. (2011) demonstrated that monsoon-generated GWs in this region could be observed from HIRDLS satellite measurements.

The $\mathrm{MF_x}$ of GWs detected using the amplitude cutoff method (panels g – i) show similar results across each region, with a 6 month offset for New Zealand/Tasmania. The $\mathrm{MF_x}$ is largely symmetrical, with and increase in detected GWs with ~ 5 mPa $\mathrm{MF_x}$ during local summer months, and a consistent lack of activity around 0 mPa, as discussed in Figure 4.

The $\mathrm{MF_x}$ calculated from GWs detected using the neighbourhood method (panels j – l) shows mainly negative $\mathrm{MF_x}$ during the winter for the Rocky Mountains and New Zealand/Tasmania (panels j & l), which corresponds with westward propagation of the GWs against the background wind. $\sim 88\%$ of waves detected using the neighbourhood method during the winter over the Rocky Mountains have a negative (westward) $\mathrm{MF_x}$. The $\mathrm{MF_x}$ for North Africa in wintertime has a near-Gaussian distribution, which is not observed in the other regions analysed. The absolute values of $\mathrm{MF_x}$ for wintertime GWs detected using the neighbourhood method over North Africa are generally lower than those in the other two regions. It is found that the $\mathrm{MF_x}$ calculated from GWs detected using the neighbourhood method are mostly larger ($\sim 10\times$) than in (Hindley et al., 2020), which could be because they used an amplitude cutoff of 0.4 K to detect GWs, so would incorporate more lower amplitude signals, bringing the mean $\mathrm{MF_x}$ lower.

The $\mathrm{MF_x}$ calculated from GWs detected using the neighbourhood method during local summer is mainly positive (eastward) for every region, although the Rocky Mountains (panel j) has a lower proportion of low value $\mathrm{MF_x}$ than the other two regions.

We next consider Figure 7, which shows polar histograms of wave phase propagation angle over the three regions for waves detected using the amplitude cutoff (panels a – c) and for waves detected using the neighbourhood method (panels d – f) during local wintertime. Panels a & d show results from the Rocky Mountains, panels b & e from North Africa, and panels c & f from New Zealand/Tasmania.

We primarily expect the waves to propagate against the background wind (Alexander et al., 2009; Hindley et al., 2020), which is generally eastwards for each of the regions during this time. This is due to the presence of the lower stratospheric polar night jet over the Rocky Mountains and New Zealand/Tasmania. Waves observed over these regions should primarily

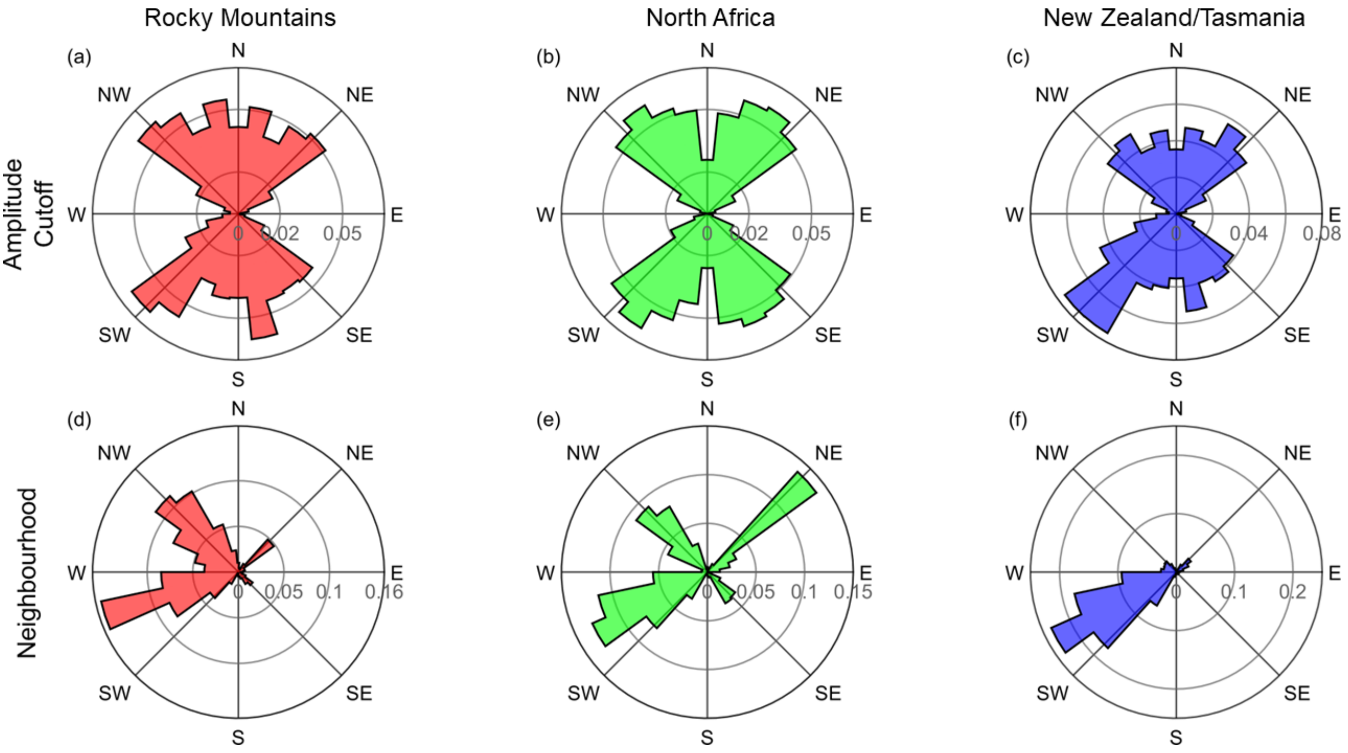

Figure 7. Polar histograms of the angles of wave phase propagation over the Rocky Mountains, North Africa, and New Zealand/Tasmania in local winter (NDJF for the Rocky Mountains and North Africa, and JJAS for New Zealand/Tasmania). Panels a – c show wave phase propagation angles for waves detected using the amplitude cutoff method, and panels d – f show wave phase propagation angles for waves detected using the neighbourhood method. Each histogram is normalised to sum to one.

be propagating westwards. This is not seen when using the amplitude cutoff method (panels a – c), which exhibits a nearly uniform spread of propagation direction across each region.

The wave phase propagation angles for GWs detected using the neighbourhood method over the Rocky Mountains (panel d) are all approximately westwards, with the spread in values being potentially due to the Rocky Mountains not being a straight ridge (such as the Andes). The spread could also be due to the movement of the lower stratospheric polar night jet throughout the local wintertime.

A similar spread in west-southwest phase propagation angles is seen for waves over North Africa (panel e), although there are many waves that propagate north eastwards too. The prevailing winds over North Africa during this time are flowing eastwards at the altitude of this study, found using ERA5 climatological reanalyses, but the southern edges of the region are within the area of the African easterly jet, which could account for the waves propagating westwards.

The tight spacing between the most south-westward waves for panel f (New Zealand/Tasmania) indicates that these waves propagate into the wind. This agrees with the findings of Smith et al. (2016), Jiang et al. (2019) and Pautet et al. (2019), whose results found that most GWs from New Zealand and Tasmania travel upwind, with wavefronts nearly perpendicular to the Southern Alps. Using ERA5 climatological reanalysis data, we found that the winds in this region during this period are directed north-eastwards, which agrees with these results. These findings can be seen when using the amplitude cutoff method as well (panel c), but they are surrounded by other, potentially noise-driven, results. 33% of waves detected using the amplitude cutoff approach propagate in the south-westward direction, compared to 76% of waves detected using the neighbourhood method.

Each panel in Figure 7 exhibits a distinctive bias where relatively few waves are seen propagating in the eastward and westward direction. This is due to an underlying bias in our ST analysis, which is due to the across-track fourth-order polynomial used to remove long wavelength background signatures, along with wavelength restrictions imposed upon the ST. These restrictions, coupled with the different resolutions in the across- and along-track directions, create this bias. The fourth-order polynomial method for removing the background signatures is the standard, identifying a new method for this remains a subject of future work.

5 Conclusions

In this study, a method for the detection of stratospheric GWs in AIRS/Aqua observations was developed, which we refer to as the "neighbourhood method". This uses a variant of the 3D S-transform to calculate the horizontal wavenumbers of temperature perturbations, then find areas of spatially stable horizontal wavenumbers (assumed to be GWs), which allow for the creation of a binary wave-presence mask. This allows us to produce a new global climatology of GW properties and in particular identify key results accessible using this method which could not be achieved using older techniques. To quantify this, we have applied both the neighbourhood method and the existing widely-used amplitude cutoff method to 5 years of data between 2010–2014.

Analysing these data, we conclude that:

- $\sim 25\%$ of all GWs detected using the new neighbourhood method could not be detected using the older amplitude cutoff method, and would be indistinguishable from instrument noise if neither method were applied. In regions dominated by non-orographic low-amplitude GW activity, such as North Africa, this difference increases to as much as $\sim$50% of all GWs, while in other regions dominated by strong orographic waves such as the Southern Andes the fraction is lower.
- Mean GW amplitudes calculated using the neighbourhood method are generally greater than those computed using the amplitude cutoff method. An example of this is seen in Figure 2, where the maximum difference between amplitudes is ~ 3 K, a value comparable to global maximum values when neither method is applied. This large difference is consistent with the inclusion of a greater fraction of instrument noise when using the amplitude-cutoff method, which will tend to skew results towards lower values.
- The effects of the semi-annual oscillation on GW momentum flux are clearly observed around the tropics when using the neighbourhood method, but are barely visible when using an amplitude cutoff approach. The zonal momentum flux calculated using this method is $\sim 40\times$ greater than seen in Hindley et al. (2020), who applied no filtering method.

https://doi.org/10.5194/egusphere-2025-455
Preprint. Discussion started: 18 February 2025

- Mean zonal momentum fluxes for GWs detected using the neighbourhood method exhibit plausible directionality when compared to theory, especially when corroborating against ERA5 background winds.
- In general, the results produced using the neighbourhood method have a global morphology consistent with linear wave theory and consistent with that produced by the amplitude cutoff method given the known limitations of that technique. This applies at both global and regional scales.

The neighbourhood method can be used on any nadir-sounding satellite that has a reliable ST output, with minor changes to the parameters needed to get the most accurate GW detections. In particular, the outputs from the neighbourhood method could be used to make GW parameterisations in models more accurate, especially over regions of typically low-amplitude waves. In addition, they could support backwards ray-tracing of GWs, or be used as a training set for a large scale convolutional neural network. We are currently investigating the lattermost option, and plan to present it in a future study.

Appendix A: Appendix

There are two variables that must be chosen as fixed values in the neighbourhood method: the neighbourhood size, and the average difference cutoff. These must be set to maximise the amount of real GW information, but minimise the amount of noise present. The perfect values for these variables vary greatly on a case-by-case basis, so for broad application we must empirically-determine values that suit the majority of waves. A decision was made to be conservative with the size and number of waves detected, to be confident that all the waves detected have no extraneous noise, or that no noise is detected as wave signals, and we note clearly that different tuning parameters could detect more waves, but at a greater cost in terms of false positives.

A1 Neighbourhood Size

Figure A1 shows the case study described in Figure1, with four different neighbourhood sizes used for the wave detection. Using a small, 3 x 3, neighbourhood (panel a), the neighbourhood method detects too many waves, most of which cannot be seen in the temperature perturbations. Panels c (7 x 7) and d (9 x 9) appear to have stabilised around the large wave in the North, but they do not capture the GW over Central America. Only panel b (5 x 5) detects both waves visible in the temperature perturbations and no extra noise. This analysis was done for multiple other cases, and the 5 x 5 neighbourhood was chosen.

A2 Average Difference Cutoff

Using the 5×5 neighbourhood chosen in Appendix A1, the average difference cutoffs were varied. For clarity, the larger the cutoff, the more, and larger, waves would be expected to be detected. This is seen in Figure A2; panel a uses a cutoff of 0.5×10^{-4} km^{-1} and detects the smallest total area of waves, but it does not detect any noise. This was deemed to be too conservative. Panel d uses a cutoff of 0.1×10^{-2} km^{-1}, which has the same issue as in Figure A1a of detecting too many waves. Using many other cases, 2×10^{-4} km^{-1} was chosen as the average difference cutoff used on the dataset.

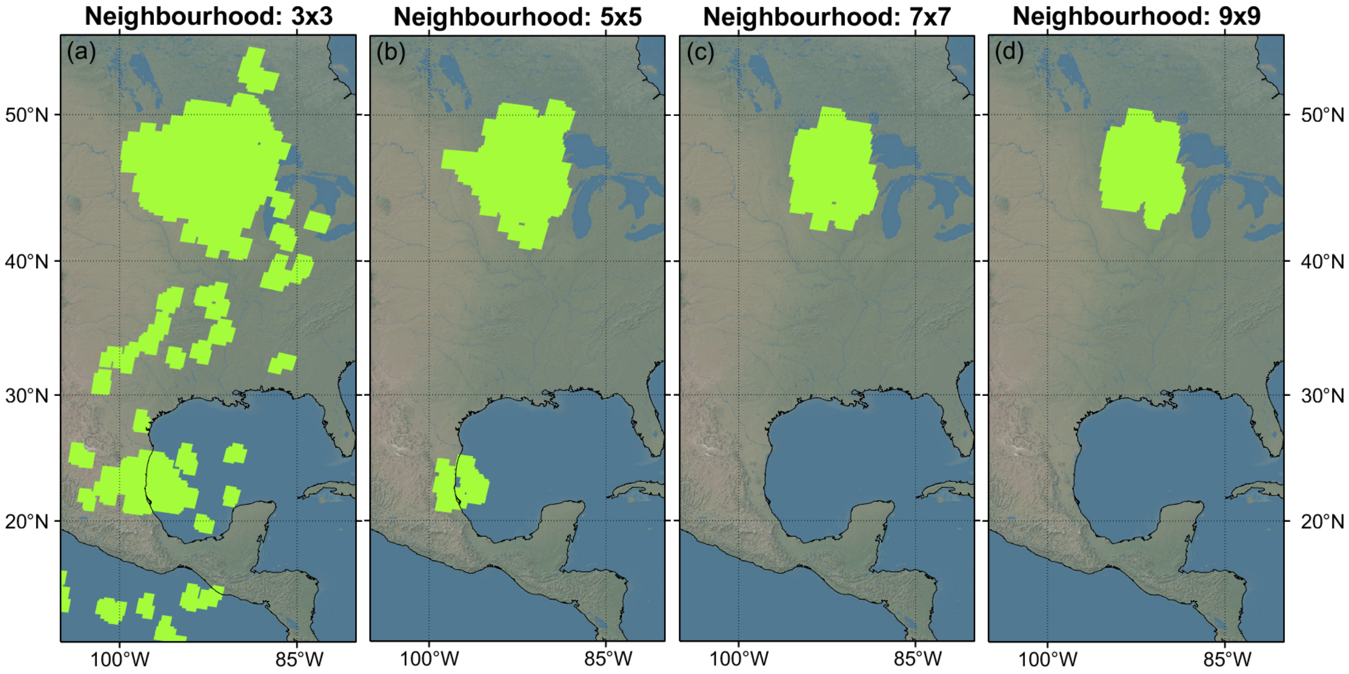

Figure A1. Various neighbourhood sizes for the case study described in the method

Data availability. The data that supported this study can be found at Hoffmann, Lars, 2021, "AIRS/Aqua Observations of Gravity Waves", https://doi.org/10.26165/JUELICH-DATA/LQAAJA, Jülich DATA, V1

Author contributions. Peter Berthelemy created the method building on the S-Transform, all the figures, and wrote the text. Neil Hindley supplied the code and the expertise for the S-Transform. Corwin Wright, Neil Hindley, and Phoebe Noble supervised the work, with necessary inputs for the direction in which to take the work. Lars Hoffmann supplied the AIRS retrieval data.

Competing interests. The authors declare that they have no conflict of interest.

Acknowledgements. Peter G. Berthelemy was supported by an URSA studentship awarded by the University of Bath and by Royal Society grant RF\ERE\210079 Corwin J. Wright was supported by Royal Society Research Fellowship URF\R\221023 and NERC grants NE/V01837X/1, NE/W003201/1 and NE/Z50399X/1. Neil P. Hindley was supported by NERC grants NE/W003201/1 and NE/Z50399X/1, and NERC Fellowship NE/X017842/1 . Phoebe E. Noble was supported by NERC grants NE/V01837X/1 and NE/W003201/1. This manuscript benefited from discussions at the International Space Science Institute in Bern as part of International Team #567.

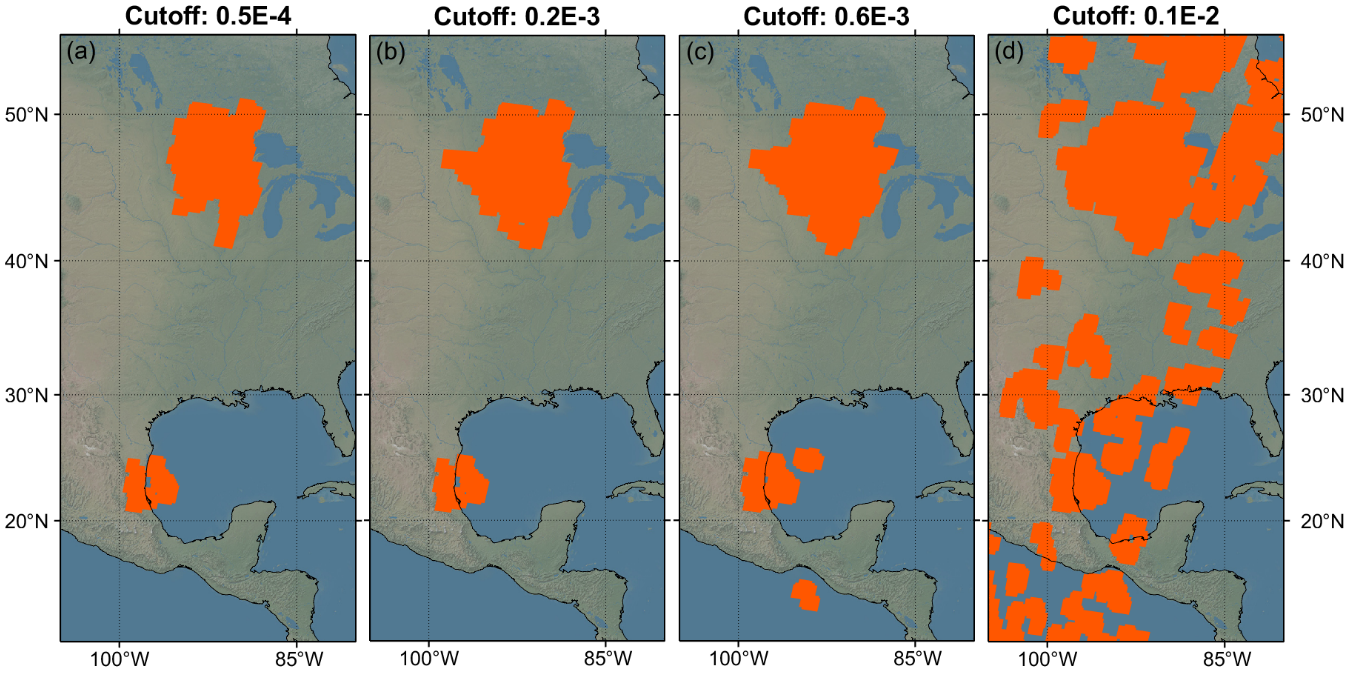

Figure A2. Various average difference cutoffs for the case study described in the method

References

Achatz, U., Alexander, M. J., Becker, E., Chun, H.-Y., Dörnbrack, A., Holt, L., Plougonven, R., Polichtchouk, I., Sato, K., Sheshadri, A., Stephan, C. C., van Niekerk, A., and Wright, C. J.: Atmospheric Gravity Waves: Processes and Parameterization, Journal of the Atmospheric Sciences, 81, 237 – 262, https://doi.org/10.1175/JAS-D-23-0210.1, 2024.

Alexander, M., Eckermann, S. D., Broutman, D., and Ma, J.: Momentum flux estimates for South Georgia Island mountain waves in the stratosphere observed via satellite, Geophysical Research Letters, 36, https://doi.org/10.1029/2009gl038587, 2009.

Alexander, M., Geller, M., McLandress, C., Polavarapu, S., Preusse, P., Sassi, F., Sato, K., Eckermann, S., Ern, M., Hertzog, A., et al.: Recent developments in gravity-wave effects in climate models and the global distribution of gravity-wave momentum flux from observations and models, Quarterly Journal of the Royal Meteorological Society, 136, 1103–1124, 2010.

Alexander, M. J. and Barnet, C.: Using Satellite Observations to Constrain Parameterizations of Gravity Wave Effects for Global Models, Journal of the Atmospheric Sciences, 64, 1652–1665, https://doi.org/10.1175/jas3897.1, 2007.

Alexander, M. J. and Teitelbaum, H.: Observation and analysis of a large amplitude mountain wave event over the Antarctic peninsula, Journal of Geophysical Research, 112, https://doi.org/10.1029/2006jd008368, 2007.

Aumann, H., Chahine, M., Gautier, C., Goldberg, M., Kalnay, E., McMillin, L., Revercomb, H., Rosenkranz, P., Smith, W., Staelin, D., Strow, L., and Susskind, J.: AIRS/AMSU/HSB on the Aqua mission: design, science objectives, data products, and processing systems, IEEE Transactions on Geoscience and Remote Sensing, 41, 253–264, https://doi.org/10.1109/TGRS.2002.808356, 2003.

Baldwin, M. P., Gray, L. J., Dunkerton, T. J., Hamilton, K., Haynes, P. H., Randel, W. J., Holton, J. R., Alexander, M. J., Hirota, I., Horinouchi, T., Jones, D. B. A., Kinnersley, J. S., Marquardt, C., Sato, K., and Takahashi, M.: The quasi-biennial oscillation, Reviews of Geophysics, 39, 179–229, https://doi.org/10.1029/1999rg000073, 2001.

Birch, C. E., Parker, D. J., O'Leary, A., Marsham, J. H., Taylor, C. M., Harris, P. P., and Lister, G. M. S.: Impact of soil moisture and convectively generated waves on the initiation of a West African mesoscale convective system, Quarterly Journal of the Royal Meteorological Society, 139, 1712–1730, https://doi.org/10.1002/qj.2062, 2012.

Booker, J. R. and Bretherton, F. P.: The critical layer for internal gravity waves in a shear flow, Journal of Fluid Mechanics, 27, 513–539, https://doi.org/10.1017/S0022112067000515, 1967.

Bossert, K., Kruse, C. G., Heale, C. J., Fritts, D. C., Williams, B. P., Snively, J. B., Pautet, P.-D., and Taylor, M. J.: Secondary gravity wave generation over New Zealand during the DEEPWAVE campaign, Journal of Geophysical Research: Atmospheres, 122, 7834–7850, https://doi.org/10.1002/2016jd026079, 2017.

Chahine, M. T., Pagano, T. S., Aumann, H. H., Atlas, R., Barnet, C., Blaisdell, J., Chen, L., Divakarla, M., Fetzer, E. J., Goldberg, M., Gautier, C., Granger, S., Hannon, S., Irion, F. W., Kakar, R., Kalnay, E., Lambrigtsen, B. H., Lee, S.-Y., Marshall, J. L., Mcmillan, W. W., Mcmillin, L., Olsen, E. T., Revercomb, H., Rosenkranz, P., Smith, W. L., Staelin, D., Strow, L. L., Susskind, J., Tobin, D., Wolf, W., and Zhou, L.: AIRS: Improving Weather Forecasting and Providing New Data on Greenhouse Gases, Bulletin of the American Meteorological Society, 87, 911–926, https://doi.org/10.1175/BAMS-87-7-911, 2006.

Chapman, C. C., Hogg, A. M., Kiss, A. E., and Rintoul, S. R.: The Dynamics of Southern Ocean Storm Tracks, Journal of Physical Oceanography, 45, 884–903, https://doi.org/10.1175/jpo-d-14-0075.1, 2015.

Choi, H. J., Chun, H. Y., Gong, J., and Wu, D. L.: Comparison of gravity wave temperature variances from ray-based spectral parameterization of convective gravity wave drag with AIRS observations, Journal of geophysical research, 117, https://doi.org/10.1029/2011jd016900, 2012.

Delisi, D. P. and Dunkerton, T. J.: Seasonal Variation of the Semiannual Oscillation, Journal of the Atmospheric Sciences, 45, 2772–2787, https://doi.org/10.1175/1520-0469(1988)045<2772:svotso>2.0.co;2, 1988.

Dunkerton, T.: Wave Transience in a Compressible Atmosphere. Part III: The Saturation of Internal Gravity Waves in the Mesophere, Journal of the atmospheric sciences, 39, 1042–1051, https://doi.org/10.1175/1520-0469(1982)039<1042:wtiaca>2.0.co;2, 1982.

Eckermann, S. and Wu, D.: Satellite detection of orographic gravity-wave activity in the winter subtropical stratosphere over Australia and Africa, Geophysical research letters, 39, 2012.

Ern, M., Preusse, P., Alexander, M. J., and Warner, C. D.: Absolute values of gravity wave momentum flux derived from satellite data, Journal of Geophysical Research: Atmospheres, 109, https://doi.org/https://doi.org/10.1029/2004JD004752, 2004.

Ern, M., Trinh, Q. T., Kaufmann, M., Krisch, I., Preusse, P., Ungermann, J., Zhu, Y., Gille, J. C., Mlynczak, M. G., Russell, III, J. M., Schwartz, M. J., and Riese, M.: Satellite observations of middle atmosphere gravity wave absolute momentum flux and of its vertical gradient during recent stratospheric warmings, ATMOSPHERIC CHEMISTRY AND PHYSICS, 16, 9983–10 019, https://doi.org/10.5194/acp-16-9983-2016, 2016.

Ern, M., Hoffmann, L., and Preusse, P.: Directional gravity wave momentum fluxes in the stratosphere derived from high-resolution AIRS temperature data, Geophysical research letters, 44, 475–485, https://doi.org/10.1002/2016gl072007, 2017.

Ern, M., Diallo, M., Preusse, P., Mlynczak, M. G., Schwartz, M. J., Wu, Q., and Riese, M.: The semiannual oscillation (SAO) in the tropical middle atmosphere and its gravity wave driving in reanalyses and satellite observations, Atmospheric chemistry and physics, 21, 13 763–13 795, https://doi.org/10.5194/acp-21-13763-2021, 2021.

Fritts, D. C. and Alexander, M. J.: Gravity wave dynamics and effects in the middle atmosphere, Reviews of Geophysics, 41, https://doi.org/10.1029/2001rg000106, 2003.

Fritts, D. C., Smith, R. E., Taylor, M. D., Doyle, J. D., Eckermann, S. D., Dörnbrack, A., Rapp, M., Williams, B. P., Pautet, P. D., Bossert, K., Criddle, N. R., Reynolds, C. A., Reinecke, P. A., Uddstrom, M., Revell, M. J., Turner, R. E., Kaifler, B., Wagner, J., Mixa, T., Kruse, C. G., Nugent, A. D., Watson, C. D., Gisinger, S., Smith, S. M., Lieberman, R. S., Laughman, B., Moore, J. E., Brown, W. E., Haggerty, J., Rockwell, A., Stossmeister, G., Williams, S., Hernández, G., Murphy, D., Kjær, H. A., Reid, I. M., and Ma, J.: The Deep Propagating Gravity Wave Experiment (DEEPWAVE): An Airborne and Ground-Based Exploration of Gravity Wave Propagation and Effects from Their Sources throughout the Lower and Middle Atmosphere, Bulletin of the American Meteorological Society, 97, 425–453, https://doi.org/10.1175/bams-d-14-00269.1, 2016.

Gibson, P. C., Lamoureux, M. P., and Margrave, G. F.: Letter to the Editor: Stockwell and Wavelet Transforms, Journal of Fourier Analysis and Applications, 12, 713–721, https://doi.org/10.1007/s00041-006-6087-9, 2006.

Gisinger, S., Dörnbrack, A., Matthias, V., Doyle, J. D., Eckermann, S. D., Ehard, B., Hoffmann, L., Kaifler, B., Kruse, C. G., and Rapp, M.: Atmospheric Conditions during the Deep Propagating Gravity Wave Experiment (DEEPWAVE), Monthly Weather Review, 145, 4249 – 4275, https://doi.org/10.1175/MWR-D-16-0435.1, 2017.

Gong, J. and Geller, M. A.: Vertical fluctuation energy in United States high vertical resolution radiosonde data as an indicator of convective gravity wave sources, Journal of Geophysical Research: Atmospheres, 115, https://doi.org/https://doi.org/10.1029/2009JD012265, 2010.

Gong, J., Yue, J., and Wu, D. L.: Global survey of concentric gravity waves in AIRS images and ECMWF analysis, Journal of Geophysical Research: Atmospheres, 120, 2210–2228, https://doi.org/10.1002/2014jd022527, 2015.

Hindley, N. P., Smith, N. D., Wright, C. J., Rees, A. S., and Mitchell, N. J.: A two-dimensional Stockwell transform for gravity wave analysis of AIRS measurements, Atmospheric Measurement Techniques, 9, 2545–2565, https://doi.org/10.5194/amt-9-2545-2016, 2016.

Hindley, N. P., Wright, C. J., Smith, N., Hoffmann, L., Holt, L. J., Alexander, M., Moffat-Griffin, T., and Mitchell, N. J.: Gravity waves in the winter stratosphere over the Southern Ocean: high-resolution satellite observations and 3-D spectral analysis, Atmospheric Chemistry and Physics, 19, 15 377–15 414, https://doi.org/10.5194/acp-19-15377-2019, 2019.

Hindley, N. P., Wright, C. J., Hoffmann, L., Moffat-Griffin, T., and Mitchell, N. J.: An 18-Year Climatology of Directional Stratospheric Gravity Wave Momentum Flux From 3-D Satellite Observations, Geophysical research letters, 47, https://doi.org/10.1029/2020gl089557, 2020.

Hoffmann, L. and Alexander, M. J.: Retrieval of stratospheric temperatures from Atmospheric Infrared Sounder radiance measurements for gravity wave studies, Journal of Geophysical Research, 114, https://doi.org/10.1029/2008jd011241, 2009.

Hoffmann, L., Xue, X., and Alexander, M. J.: A global view of stratospheric gravity wave hotspots located with Atmospheric Infrared Sounder observations, Journal of Geophysical Research: Atmospheres, 118, 416–434, https://doi.org/10.1029/2012jd018658, 2013.

Hoffmann, L., Alexander, M., Clerbaux, C., Grimsdell, A. W., Meyer, C. I., Rößler, T., and Tournier, B.: Intercomparison of stratospheric gravity wave observations with AIRS and IASI, Atmospheric Measurement Techniques, 7, 4517–4537, https://doi.org/10.5194/amt-7-4517-2014, 2014.

Hoffmann, L., Grimsdell, A. W., and Alexander, M. J.: Stratospheric gravity waves at Southern Hemisphere orographic hotspots: 2003–2014 AIRS/Aqua observations, Atmospheric Chemistry and Physics, 16, 9381–9397, https://doi.org/10.5194/acp-16-9381-2016, 2016.

Holton, J. M.: The Role of Gravity Wave Induced Drag and Diffusion in the Momentum Budget of the Mesosphere, Journal of Atmospheric Sciences, 39, 791–799, https://doi.org/10.1175/1520-0469(1982)039<0791:trogwi>2.0.co;2, 1982.

Hájková, D. and Šácha, P.: Parameterized orographic gravity wave drag and dynamical effects in CMIP6 models, Climate dynamics, 62, https://doi.org/10.1007/s00382-023-07021-0, 2023.

475 Jiang, Q., Doyle, J. D., Eckermann, S. D., and Williams, B. P.: Stratospheric Trailing Gravity Waves from New Zealand, Journal of the atmospheric sciences, 76, 1565–1586, https://doi.org/10.1175/jas-d-18-0290.1, 2019.

Kalisch, S., Chun, H.-Y., Ern, M., Preusse, P., Trinh, Q. T., Eckermann, S. D., and Riese, M.: Comparison of simulated and observed convective gravity waves, Journal of Geophysical Research: Atmospheres, 121, 13,474–13,492, https://doi.org/10.1002/2016jd025235, 2016.

480 Lear, E. J., Wright, C. J., Hindley, N., Polichtchouk, I., and Hoffmann, L.: Comparing gravity waves in a kilometre-scale run of the IFS to AIRS satellite observations and ERA5, https://doi.org/10.22541/essoar.169755196.69126430/v1, 2023.

Lehmann, C. I., Kim, Y.-H., Preusse, P., Chun, H.-Y., Ern, M., and Kim, S.-Y.: Consistency between Fourier transform and small-volume few-wave decomposition for spectral and spatial variability of gravity waves above a typhoon, Atmospheric Measurement Techniques, 5, 1637–1651, https://doi.org/10.5194/amt-5-1637-2012, 2012.

485 Lilly, D. K. and Kennedy, P. T. F.: Observations of a Stationary Mountain Wave and its Associated Momentum Flux and Energy Dissipation, Journal of the Atmospheric Sciences, 30, 1135–1152, https://doi.org/10.1175/1520-0469(1973)030<1135:ooasmw>2.0.co;2, 1973.

Marshall, J. L., Jung, J. A., Derber, J., Chahine, M. T., Treadon, R., Lord, S. J., Goldberg, M. D., Wolf, W., Liu, H. C., Joiner, J., Woollen, J. S., Todling, R., van Delst, P., and Tahara, Y.: Improving Global Analysis and Forecasting with AIRS, Bulletin of the American Meteorological Society, 87, 891–895, https://doi.org/10.1175/bams-87-7-891, 2006.

490 Orza, J., Dhital, S., Fiedler, S., and Kaplan, M.: Large scale upper-level precursors for dust storm formation over North Africa and poleward transport to the Iberian Peninsula. Part I: An observational analysis, Atmospheric Environment, 237, 117 688, https://doi.org/10.1016/j.atmosenv.2020.117688, 2020.

Pautet, P.-D., Taylor, M. J., Eckermann, S. D., and Criddle, N. R.: Regional Distribution of Mesospheric Small-Scale Gravity Waves During DEEPWAVE, Journal of geophysical research. Atmospheres, 124, 7069–7081, https://doi.org/10.1029/2019jd030271, 2019.

495 Plougonven, R. and Teitelbaum, H.: Comparison of a large-scale inertia-gravity wave as seen in the ECMWF analyses and from radiosondes, Geophysical Research Letters, 30, https://doi.org/10.1029/2003gl017716, 2003.

Preusse, P., Dörnbrack, A., Eckermann, S. D., Riese, M., Schaeler, B., Bacmeister, J. T., Broutman, D., and Grossmann, K. U.: Space-based measurements of stratospheric mountain waves by CRISTA 1. Sensitivity, analysis method, and a case study, Journal of Geophysical Research: Atmospheres, 107, CRI 6–1–CRI 6–23, https://doi.org/10.1029/2001jd000699, 2002.

500 Sato, K., Tateno, S., Watanabe, S., and Kawatani, Y.: Gravity Wave Characteristics in the Southern Hemisphere Revealed by a High-Resolution Middle-Atmosphere General Circulation Model, Journal of the Atmospheric Sciences, 69, 1378 – 1396, https://doi.org/10.1175/JAS-D-11-0101.1, 2012.

Smith, A. K. and Lyjak, L. V.: An observational estimate of gravity wave drag from the momentum balance in the middle atmosphere, Journal of geophysical research, 90, 2233–2241, https://doi.org/10.1029/jd090id01p02233, 1985.

505 Smith, A. K., Garcia, R. R., Moss, A. C., and Mitchell, N. J.: The Semiannual Oscillation of the Tropical Zonal Wind in the Middle Atmosphere Derived from Satellite Geopotential Height Retrievals, Journal of the atmospheric sciences, 74, 2413–2425, https://doi.org/10.1175/jas-d-17-0067.1, 2017.

Smith, R. B., Nugent, A. D., Kruse, C. G., Fritts, D. C., Doyle, J. D., Eckermann, S. D., Taylor, M. J., Dörnbrack, A., Uddstrom, M., Cooper, W., et al.: Stratospheric gravity wave fluxes and scales during DEEPWAVE, Journal of the Atmospheric Sciences, 73, 2851–2869, 2016.

Stockwell, R., Mansinha, L., and Lowe, R.: Localization of the complex spectrum: the S transform, IEEE Transactions on Signal Processing, 44, 998–1001, https://doi.org/10.1109/78.492555, 1996.

Trinh, P. H.: A topological study of gravity free-surface waves generated by bluff bodies using the method of steepest descents, Proceedings - Royal Society. Mathematical, physical and engineering sciences, 472, 20150 833–20150 833, https://doi.org/10.1098/rspa.2015.0833, 2016.

Tsuda, T., Murayama, Y., Wiryosumarto, H., Harijono, S. W. B., and Kato, S.: Radiosonde observations of equatorial atmosphere dynamics over Indonesia: 2. Characteristics of gravity waves, Journal of geophysical research, 99, 10 507–10 507, https://doi.org/10.1029/94jd00354, 1994.

Wang, L. and Geller, M. A.: Morphology of gravity-wave energy as observed from 4 years (1998–2001) of high vertical resolution U.S. radiosonde data, Journal of Geophysical Research, 108, ACL 1–12, https://doi.org/10.1029/2002jd002786, 2003.

Whiteway, J. A. and Duck, T. J.: Evidence for critical level filtering of atmospheric gravity waves, Geophysical Research Letters, 23, 145–148, https://doi.org/https://doi.org/10.1029/95GL03784, 1996.

Wright, C. J. and Banyard, T. P.: Multidecadal Measurements of UTLS Gravity Waves Derived From Commercial Flight Data, Journal of Geophysical Research: Atmospheres, 125, e2020JD033 445, https://doi.org/https://doi.org/10.1029/2020JD033445, e2020JD033445 10.1029/2020JD033445, 2020.

Wright, C. J., Hindley, N. P., Moss, A. C., and Mitchell, N. J.: Multi-instrument gravity-wave measurements over Tierra del Fuego and the Drake Passage – Part 1: Potential energies and vertical wavelengths from AIRS, COSMIC, HIRDLS, MLS-Aura, SAAMER, SABER and radiosondes, Atmospheric Measurement Techniques, 9, 877–908, https://doi.org/10.5194/amt-9-877-2016, 2016.

Wright, C. J., Hindley, N. P., Hoffmann, L., Alexander, M. J., and Mitchell, N. J.: Exploring gravity wave characteristics in 3-D using a novel S-transform technique: AIRS/Aqua measurements over the Southern Andes and Drake Passage, Atmospheric Chemistry and Physics, 17, 8553–8575, https://doi.org/10.5194/acp-17-8553-2017, 2017.

Wright, C. J., Hindley, N. P., Alexander, M. J., Holt, L., and Hoffmann, L.: Using vertical phase differences to better resolve 3D gravity wave structure, Atmospheric Measurement Techniques, 14, 5873–5886, https://doi.org/10.5194/amt-14-5873-2021, 2021.

Wright, J. S., Fu, R., Fueglistaler, S., Liu, Y. S., and Zhang, Y.: The influence of summertime convection over Southeast Asia on water vapor in the tropical stratosphere, Journal of Geophysical Research: Atmospheres, 116, https://doi.org/https://doi.org/10.1029/2010JD015416, 2011.

Wu, D. L.: Mesoscale gravity wave variances from AMSU-A radiances, Geophysical Research Letters, 31, n/a–n/a, https://doi.org/10.1029/2004gl019562, 2004.

Zhang, F., Zhang, M., Wei, J., and Wang, S.: Month-long simulations of gravity waves over North America and North Atlantic in comparison with satellite observations, Acta Meteorologia Sinica/Acta Meteorologica Sinica, 27, 446–454, https://doi.org/10.1007/s13351-013-0301-x, 2013.

Zhang, F., Wei, J., Zhang, R., Bowman, K. W., Pan, L., Atlas, E., and Wofsy, S. C.: Aircraft measurements of gravity waves in the upper troposphere and lower stratosphere during the START08 field experiment, Atmospheric chemistry and physics, 15, 7667–7684, https://doi.org/10.5194/acp-15-7667-2015, 2015.

Zhang, S. D.: A numerical study on the propagation and evolution of resonant interacting gravity waves, Journal of geophysical research, 109, https://doi.org/10.1029/2004jd004822, 2004.